Nonlinear cosmological spherical collapse of quintessence

Rekier, Jérémy; Füzfa, André; Cordero-Carrión, I.

Published in:
Physical review D

DOI:
10.1103/PhysRevD.93.043533

Publication date:
2016

Document Version
Publisher's PDF, also known as Version of record

PHYSICAL REVIEW D **93,** 043533 (2016)

Nonlinear cosmological spherical collapse of quintessence

J. Rekier,[1,*] A. Füzfa,[1] and I. Cordero-Carrión[2]

[1]*Namur Centre for Complex Systems (naXys), University of Namur, B-5000 Namur, Belgium*
[2]*Departamento de Matemática Aplicada, Universidad de Valencia, E-46100 Burjassot, Spain*

(Received 30 September 2015; published 17 February 2016)

We present a study of the fully relativistic spherical collapse in the presence of quintessence using on numerical relativity, following the method proposed by the authors in a previous article [Phys. Rev. D 91, 024025 (2015)]. We ascertain the validity of the method by studying the evolution of a spherically symmetric quintessence inhomogeneity on a de Sitter background and we find that it has an impact on the local expansion around the center of coordinates. We then proceed to compare the results of our method to those of the more largely adopted *top-hat* model. We find that quintessence inhomogeneities do build up under the effect that matter inhomogeneities have on the local space-time, yet remain very small due to the presence of momentum transfer from the over-dense to the background regions. We expect that these might have an even more important role in modified theories of gravitation.

DOI: 10.1103/PhysRevD.93.043533

I. INTRODUCTION

In a companion paper [1], we proposed a method based on techniques of numerical relativity to compute the collapse of a matter over-density on the expanding space-time background. In the present article, this method is extended in order to incorporate the effects of quintessence modeled as a real scalar field.

The late-time acceleration of the expansion of the Universe is validated by many independent observations including the *type Ia supernova diagram* [2–6], angular fluctuations of the *cosmic microwave background* [7,8] and *galaxy redshift distortion* [9]. One can explain this acceleration by *fine-tuning* the value of a cosmological constant Λ. There is, however, a number of conceptual problems [10] associated with this that have led many to consider other options. Among these is the hypothesis that the late-time acceleration is due to the dynamics of a new variety of energy called *quintessence* [11–13]. In this framework, the study of the formation of large-scale structure performed with N-body simulations is a very interesting topic as it allows one to draw important conclusions on the dynamics of the homogeneous Universe and the nature of the quintessence component [14–16]. All of these studies rely on simplified models of collapse of local inhomogeneities.

Some groups have investigated the collapse in the presence of quintessence using the top-hat formalism[1] [17–22]. Some investigated the case where quintessence is due to a real scalar field [23–25]. However, the top-hat model can only be somewhat motivated as a limit case of the *Lemaître-Tolman-Bondi* (LTB) solution valid for pressureless matter only and, in spite of its successes, is not a rigorous solution of Einstein's equations in the general case.

In most works, it is argued that quintessence should not cluster on astrophysical scales and contributes only to the background dynamics. The method that we have developed allows us to test this hypothesis. It also allows us to investigate the evolution and effects of the anisotropic stress due to the presence of quintessence on the formation of structure beyond the perturbation level which constitutes a good test on the nature of quintessence [26,27]. The fully relativistic nonperturbative approach proposed uses tools from numerical relativity applied to the evolution of cosmological space-times with a scalar field following the early work by Shibata *et al.* [28] as well as more recent works in the field [29,30]. We highlight the role played by the momentum transfer associated with the quintessence field.

The paper is organized as follows. In Sec. II, we review the top-hat model with quintessence. The formalism that we used to solve for the fully relativistic solution is adapted from our previous work [1] and is detailed in Secs. III and IV. The validity of this is first tested in the case of a de Sitter universe filled with inhomogeneities in quintessence only. This is the subject of Secs. V and VI, which are concerned with a comparison with the top-hat model and a more detailed study that goes beyond the results from the top-hat model, respectively. Conclusions and perspectives are discussed in Sec. VII.

II. THE TOP-HAT MODEL

In the top-hat model, space-time and the matter distribution are kept piecewise homogeneous. The universe is divided into an inner and an outer region each following its own Friedmann equation [17,31,32]:

*jeremy.rekier@observatory.be

[1]By "top-hat" we understand a certain type of model in which the total energy density profile remains a step function throughout the whole evolution. The whole space-time consists only of two parts at all times and not just initially.

$$\left(\frac{\dot{a}}{a}\right)^2 = \frac{8\pi}{3}\bar{\rho}, \tag{1}$$

$$\left(\frac{\dot{R}}{R}\right)^2 = \frac{8\pi}{3}\bar{\rho}(1+\delta) - \frac{k}{R^2}, \tag{2}$$

where $a(t)$ and $R(t)$ are, respectively, the outer and inner scale factors and $\cdot$ denotes the time derivative. The density of the inner region is written in terms of the background density $\bar{\rho}$ and the density contrast δ. It is customary to assume that the background space-time is spatially flat. Note that the spatial curvature of the inner space-time k cannot in general be assumed to be a constant [32]. The energy densities inside and outside of the over-dense region each follow a conservation equation:

$$\frac{d}{dt}\bar{\rho} + 3\frac{\dot{a}}{a}(\bar{\rho}(1+w)) = 0, \tag{3}$$

$$\frac{d}{dt}(\bar{\rho}(1+\delta)) + 3\frac{\dot{R}}{R}[\bar{\rho}(1+\delta)(1+w)] = \Gamma, \tag{4}$$

where the species is assumed to follow an equation of state of the form $p = w\rho$. The function Γ is an adjustable parameter depending on whether the considered species is allowed to cluster. Many researchers have argued that the quintessence component of the universe should remain homogeneous at all times [23,33,34]. This argument is based on the equation for the evolution of scalar field perturbations in the matter-dominated era [34],

$$\delta\ddot{\phi} + 3H\delta\dot{\phi} + (k^2/a^2 + V_{,\phi\phi})\delta\phi = \dot{\phi}\dot{\delta}_m, \tag{5}$$

where ϕ, $\delta\phi$, δ_m, V, and $V_{,\phi\phi}$ are, respectively, the quintessence scalar field, the field perturbation, the matter over-density, the scalar field potential, and its second derivative with respect to ϕ. Equation (5) shows that there is a characteristic comoving mode $k_J/a \sim V_{,\phi\phi}$ below which the perturbations grow exponentially, corresponding to a typical length $\lambda_J \sim 1/\sqrt{V_{\phi\phi}}$, sometimes referred to as the *Jeans length*. As for most quintessential potentials, this length is larger than the horizon, and it is generally assumed that quintessence does not cluster. However, the process preventing the clustering is not explained.

Returning to the top-hat equations, in the case where the energy density is that of a scalar field with potential V, Eq. (4) reduces to

$$\ddot{\phi}_{\rm loc} + 3\frac{\dot{R}}{R}\dot{\phi}_{\rm loc} + \frac{dV}{d\phi} = \Gamma/\dot{\phi}_{\rm loc}, \tag{6}$$

where $\phi_{\rm loc}$ is the local value of the field within the over-dense region. To prevent the field from collapsing, the phenomenological functional parameter Γ must be set to [23]

$$\Gamma = -3\left(\frac{\dot{a}}{a} - \frac{\dot{R}}{R}\right)\dot{\phi}^2_{\rm loc}. \tag{7}$$

This makes the equation for the field inside the over-dense region strictly equivalent to that for the outside region, thus forcing $\phi = \phi_{\rm loc}$. In practice, this amounts to demanding that the field within the local region couples to the value taken by the expansion factor outside the region rather than the local $\frac{\dot{R}}{R}$.

The top-hat model is purely phenomenological and not a rigorous solution of the equations of general relativity. In the presence of dust matter only, the spherically symmetric cosmological solution of Einstein's equations is the LTB metric of which the top-hat model is a limit case [1]. This model is not valid in the case of a general fluid with pressure momentum transfer. Such is the case for quintessence.

The fully consistent relativistic treatment calls for numerical methods. Lasky *et al.* have made a step toward the generalization of the LTB solution by formulating the problem as an initial value problem [35]. We follow another approach based on the many successes of numerical relativity.

III. FORMALISM

Following the work presented in Ref. [1], we use the Baumgarte-Shapiro-Shibata-Nakamura (BSSN) formalism [36–38] and write the spherically symmetric squared line element as

$$ds^2 = -(\alpha^2 - \beta^2)dt^2 + 2\beta dt dr + \psi^4 a^2(t)(\hat{a}dr^2 + \hat{b}r^2 d\Omega^2), \tag{8}$$

where $\alpha(t,r)$ is the lapse, $\beta(t,r)$ is the radial component of the shift β_μ, and $\hat{a}$ and $\hat{b}$ denote the nonzero components of the diagonal conformal 3-metric. $\psi^2 a$ is the conformal factor.[2] We have factored out the cosmological scale factor $a(t)$ which follows its own dynamics that serves as dynamical background. The extrinsic curvature is split into its trace K and its conformally scaled trace-free part $\hat{A}_{\mu\nu}$,

$$K_{ij} = \frac{1}{3}\gamma_{ij}K + \psi^4 a^2 \hat{A}_{ij}, \tag{9}$$

with γ_{ij} being the spatial 3-metric. Due to spherical symmetry, $\hat{A}_{ij}$ has only two nonzero components: $A_a := \hat{A}^r_r$ and $A_b := \hat{A}^\theta_\theta$. As $\hat{A}_{ij}$ is traceless, one further has $A_a + 2A_b = 0$. The BSSN formalism ensures that

[2]The denomination of $\psi\sqrt{a}$ as the *conformal factor* is customary in general relativity (see, e.g., Refs. [39,40]). It differs from the usual expression $\bar{g}_{\mu\nu} = \Omega^2\eta_{\mu\nu}$ with Ω being the conformal factor (see, e.g., Ref. [41]) by a power of 2. Both definitions are used interchangeably in Ref. [42].

$\det(\gamma_{ij})/(\psi^2 a)^3 = \det(f_{ij})$ at all times, where f_{ij} is the flat metric which here translates to $\hat{a}\hat{b}^2 = 1$.

For our purpose, we shall limit ourselves to the zero-shift gauge $\beta = 0$. There is no formal difficulty in choosing a different gauge. This one however allows us to perform comparisons between cosmological models more straightforwardly. The normal vector which is tangent to the worldline of the Eulerian observer reads $n_\mu = (-\alpha, 0, 0, 0)$. The set of dynamical and constraint equations was given in Ref. [1]. The source terms are

$$\begin{aligned} E &\coloneqq n_\alpha n_\beta T^{\alpha\beta}, \\ j_i &\coloneqq -\gamma_{i\alpha} n_\beta T^{\alpha\beta}, \\ S_{ij} &\coloneqq \gamma_{\alpha i}\gamma_{\beta j} T^{\alpha\beta}, \end{aligned} \tag{10}$$

where E is the energy density as seen by the Eulerian observer, j_i is the momentum transfer, and S_{ij} is the stress tensor. In spherical symmetry and using adapted coordinates

$$S_{ij} = \begin{pmatrix} S_{rr} & & \\ & S_{\theta\theta} & \\ & & S_{\theta\theta} \end{pmatrix}, \qquad j_i = (j_r(t,r), 0, 0). \tag{11}$$

We further define $Sa \coloneqq S^r_r$ and $Sb \coloneqq S^\theta_\theta$. The dynamics of the quintessence field is given by the Klein-Gordon equation

$$\partial_\mu((-g)^{1/2}\partial^\mu\phi) = (-g)^{1/2}\partial_\phi V, \tag{12}$$

where $g = \det(g_{\mu\nu})$, the determinant of the complete metric. In order to write this as a first-order system, one defines [29]

$$\Pi \coloneqq n_\mu \partial^\mu \phi, \tag{13}$$

$$\Psi_i \coloneqq \partial_i \phi. \tag{14}$$

Assuming spherical symmetry, the evolution equations for the quintessence field and the related variables (13) and (14) can be written as (using the shorthand $\Psi \equiv \Psi_r$)

$$\pounds_n \phi = \Pi, \tag{15}$$

$$\pounds_n \Psi = \frac{1}{\alpha}\partial_r(\alpha\Pi), \tag{16}$$

$$\pounds_n \Pi = K\Pi + \frac{1}{\alpha} D_r(\alpha\Psi) - \frac{dV}{d\phi}. \tag{17}$$

In the presence of both matter and a scalar field, the energy source functions have two components. The expressions for the scalar field components read

$$E_\phi = \frac{1}{2}\left(\Pi^2 + \frac{\Psi^2}{\psi^4 a^2 \hat{a}}\right) + V, \tag{18}$$

$$S^\phi_a = \frac{1}{2}\left(\Pi^2 + \frac{\Psi^2}{\psi^4 a^2 \hat{a}}\right) - V, \tag{19}$$

$$S^\phi_b = \frac{1}{2}\left(\Pi^2 - \frac{\Psi^2}{\psi^4 a^2 \hat{a}}\right) - V, \tag{20}$$

$$j^\phi_r = -\Pi\Psi. \tag{21}$$

In the zero-shift gauge, the evolution equations reduce to (making use of $\hat{a}\hat{b}^2 = 1$).

$$\partial_t \Pi = \alpha K \Pi - \frac{1}{\psi^6 a^2 r^2}\partial_r\left(\alpha \frac{\psi^2 r^2}{\hat{a}}\Psi\right) - \alpha\frac{dV}{d\phi}, \tag{22}$$

$$\partial_t \Psi = \partial_r(\alpha\Pi), \tag{23}$$

$$\partial_t \phi = \alpha\Pi. \tag{24}$$

The numerical solution for the dynamics is obtained in a way similar to what was presented in Ref. [1] using a second-order *partially implicit Runge-Kutta* (PIRK) method [43,44]; more details can be found in the Appendix. The radial dimension is approximated by a uniformly discretized cell-centered grid, and radial derivatives are computed with a fourth-order finite difference scheme. We use fourth-order Kreiss-Oliger dissipation. A few virtual points of negative radius are added to the numerical grid to ensure that the numerical profiles have the correct parity throughout the integration.

The entire code used to produce the simulations presented in this work has been made publicly available on the web at http://github.com/jrekier/FORTCosmoSS.

The evolution of the background follows the Friedmann and acceleration equations

$$\frac{1}{\alpha_{\rm bkg}^2}\left(\frac{\dot{a}}{a}\right)^2 = \frac{8\pi}{3}\bar{\rho}, \tag{25}$$

$$\frac{1}{\alpha_{\rm bkg}^2}\frac{\ddot{a}}{a} - \frac{\dot{a}}{a}\frac{\dot{\alpha}_{\rm bkg}}{\alpha_{\rm bkg}} = -\frac{8\pi}{6}\bar{\rho}(1+3w), \tag{26}$$

where $\alpha_{\rm bkg}$ is the background value of the lapse function.

We impose radiative conditions at the outer boundary

$$\partial_t f = \partial_t f_{\rm bkg} - v\partial_r f - \frac{v}{r}(f - f_{\rm bkg}), \tag{27}$$

where v is the speed of propagation of the variable f on the grid. This is inferred by considering the characteristic structure of the variables of the evolution system of equations. $f_{\rm bkg}(t)$ denotes the spatially homogeneous

asymptotic cosmological value of the variable f and $\partial_t f_{\rm bkg}$ is its first time derivative.

We work in natural units with $G = c = 1$. In order for the complete set of units to be dimensionless, we further impose the value of the Hubble factor measured today to be equal to some adjustable parameter, $H_0 = x t_{\rm scale}^{-1}$. A comparison with the experimental value ~ 70 km/s/Mpc fixes the time scale. The length and mass scales are then obtained from $l_{\rm scale} = c t_{\rm scale}$ and $m_{\rm scale} = (c^3/G) t_{\rm scale}$. One can dispose of the need to specify the particular set of scales employed within a computation by expressing these in terms of H_0.

We consider two different dark energy models besides the simplistic ΛCDM. The first one is the inverse power-law *Ratra-Peebles* (RP) model [12] characterized by the potential

$$V(\phi) = \frac{M^{4+n}}{\phi^n}, \tag{28}$$

where n and M are constants. This produces late-time cosmological acceleration. In the general case where the field is not at rest initially, the slow-roll conditions are not satisfied at initial time as the field starts with a small value corresponding to a steep region of the potential. When it is present, the dust matter density dominates over the energy density and the universe assumes a power-law expansion in time, $a \sim t^{2/3}$, during which ϕ rolls down its potential. The field eventually comes to the flat tail region of the potential where the weak energy condition ($w < -1/3$) is violated leading to a de Sitter expansion phase. If the field is initially at rest, the evolution proceeds in the same way but starts with another de Sitter phase.

The other quintessence model considered is the *pseudo-Nambu-Goldstone boson* model (PNGB) [45]. While the RP model is an example of a *freezing* model where the violation of the weak energy condition happens at late time, the PNGB is classified within the set of *thawing* models in which this violation happens at early times [46]. The analytical expression for the PNGB potential is

$$V(\phi) = \mu^4 \cos(1 + \phi/f). \tag{29}$$

IV. SCALAR FIELD EVOLUTION

In order to test the stability and convergence properties of our method, we start by considering the evolution of a spatial distribution of scalar field in a way similar to what was performed for the analysis of the gauge dynamics in Rekier *et al.* [1]. The purpose of the background dynamics of this section is merely to allow us to test our method on a de Sitter background and is by no means to reproduce the measured expansion. The initial quintessence profile is

$$\phi = \phi_{\rm bkg}(1 + \delta\phi), \tag{30}$$

$$\delta\phi(t = 0, r) = \frac{\delta\phi_0 r^2}{1 + r^2}\left[e^{-\frac{(r-r_i)^2}{\sigma_i^2}} + e^{-\frac{(r+r_i)^2}{\sigma_i^2}}\right], \tag{31}$$

where $\delta\phi_0$ sets the initial amplitude of the pulse, r_i is its initial position, and σ_i is its spatial extension. The background value is chosen as the solution of

$$H_i^2 = \frac{8\pi}{3} V(\phi_{\rm bkg}), \tag{32}$$

which is just the Friedmann equation with $\alpha = 1$. The initial data are set after imposing

$$\hat{a}(t = 0) = \hat{b}(t = 0) = 1, \tag{33}$$

$$K(t = 0) = -3H_i, \qquad A_a(t = 0) = A_b(t = 0) = 0. \tag{34}$$

This reduces the Hamiltonian constraint to

$$a^{-2}\psi^{-5}\left(\partial_r^2\psi + \frac{2}{r}\partial_r\psi\right) + 6H_i^2 = 16\pi E_\phi, \tag{35}$$

which is solved at initial time as a boundary value problem. We perform two simulations with each one corresponding to a different value of the initial expansion factor. These are performed with the RP potential with $n = 2$. The mass scale M is chosen in order for the field to reproduce the behavior of a cosmological constant when the field has a value around $\phi_0 \sim \sqrt{8\pi}$ [46]:

$$8\pi V(\phi_0) = \Lambda. \tag{36}$$

The initial amplitude of the scalar field inhomogeneity parameters are $\delta\phi_0 = 5 \times 10^{-4}$, $\sigma = 2$, and $r_i = 20$. The field is assumed to be initially at rest [$\Pi(t = 0) = 0$]. Equation (35) then turns into

$$a^{-2}\psi^{-5}\left(\partial_r^2\psi + \frac{2}{r}\partial_r\psi\right) + 6H_i^2 = 8\pi\left(\frac{\Psi^2}{\psi^4 a^2 \hat{a}}\right) + 16\pi V(\phi). \tag{37}$$

We first study the evolution of the field in the case where the initial expansion factor is of the order of the present-day Hubble factor ($H_i = 5H_0$). The evolution of the scale factor and the homogeneous part of the scalar field are shown in Fig. 1. The universe starts off in a phase of de Sitter expansion as the slow-roll conditions are met at initial time. The field rapidly unfreezes as it rolls down its potential, leading to a milder expansion rate before assuming a long-lasting slow-roll regime until it eventually freezes out again at very late time. The scalar pulse propagation happens within the early de Sitter phase. The potential part of the

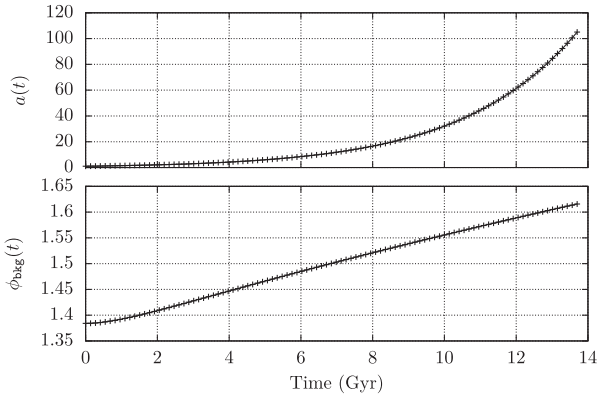

FIG. 1. Long-term cosmological evolution of the scale factor (upper panel) and background scalar field (lower panel) for a universe filled with quintessence for the Ratra-Peebles potential of Eq. (28) with $n = 2$ and the initial condition given by Eq. (36) ($H_i = 5H_0$). The field assumes a long-lasting slow-roll regime corresponding to an exponential growth of the scale factor. It is chosen to freeze out completely at very late time corresponding to $\phi \sim \sqrt{8\pi}$ (not shown in the figure).

field energy density dominates over the term proportional to the gradient of the scalar field Ψ at initial time. The evolution of the scalar field profile in the geodesic slicing is shown on Fig. 2. The scalar pulse separates into two parts. The inward-traveling pulse gets reflected from the origin of coordinates and then travels outward. The apparent dynamics is very similar to what we encountered in Ref. [1] in the study of a gauge pulse. However, the physical situation here is very different as we are now dealing with a nonvanishing distribution of energy. The situation here can be seen as the evolution of a spherical shell initially placed at a radius r_i. After the shell has bounced from the origin, the central value of the field returns to its homogeneous asymptotical value leaving no effect on the local expansion.

The violation of the Hamiltonian constraint profile is shown in Fig. 3 for the evolution in the geodesic slicing

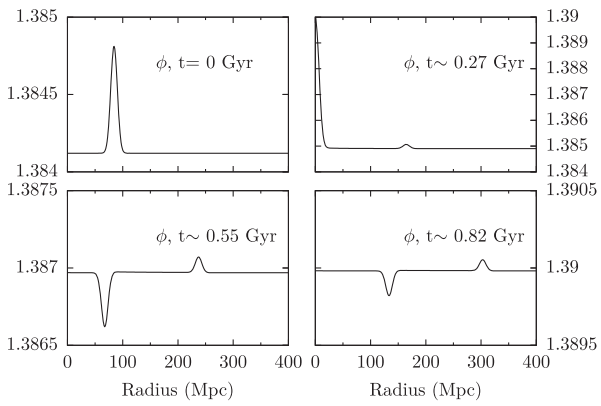

FIG. 2. Evolution of the radial profile of a Gaussian quintessence scalar pulse on a de Sitter background ($H_i = 5H_0$) for four different times ($t = 0$, 0.27, 0.55, and 0.82 Gyr).

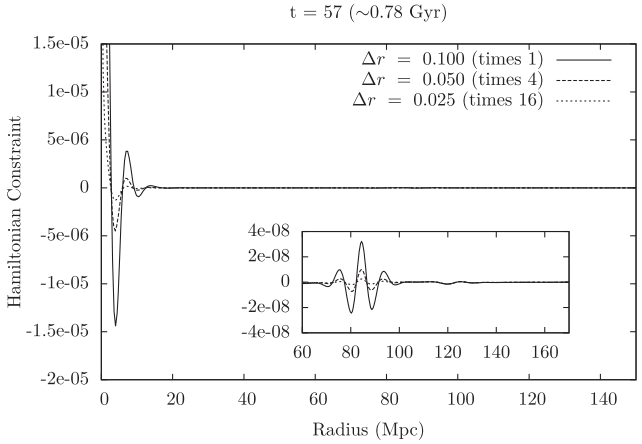

FIG. 3. Hamiltonian constraint violation profile resulting from the propagation of a Gaussian pulse in geodesic slicing for three values of the grid resolution at $t \sim 0.78$ Gyr, after the second scalar pulse has been reflected from the center of coordinates ($H_i = 5H_0$). The violation is maximal at the center of coordinates yet remains controlled throughout the integration. The rescaling of the constraint violation with resolution demonstrates that the convergence of the numerical scheme is above second order. The inset plot shows a close-up representation of the same quantity around the second scalar pulse after it has been reflected from the center of coordinates.

gauge and for three values of the resolution. The inner plot shows a close-up of the outer plot around the radius corresponding to the initial position of the scalar field pulse. A similar plot is shown for the result of the evolution in the Bona-Masso slicing with $f = 0.333$ in Fig. 4.

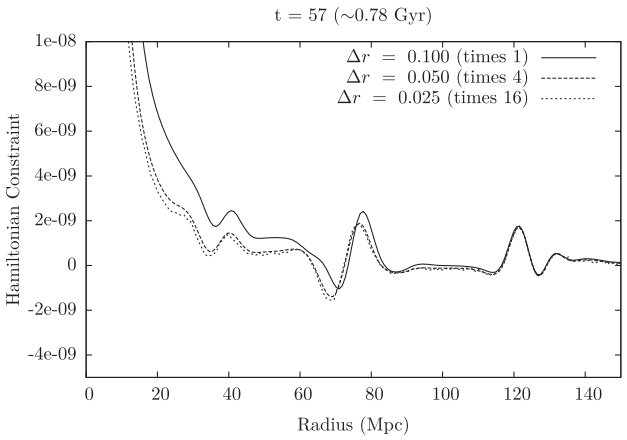

FIG. 4. Hamiltonian constraint violation profile resulting from the propagation of a Gaussian pulse in Bona-Masso slicing for three values of the grid resolution at $t \sim 0.78$ Gyr, after the second scalar pulse has been reflected from the center of coordinates ($H_i = 5H_0$). The violation is maximal at the center of coordinates yet remains controlled throughout the integration. The rescaling of the constraint violation with the resolution demonstrates that the convergence of the numerical scheme is above second order.

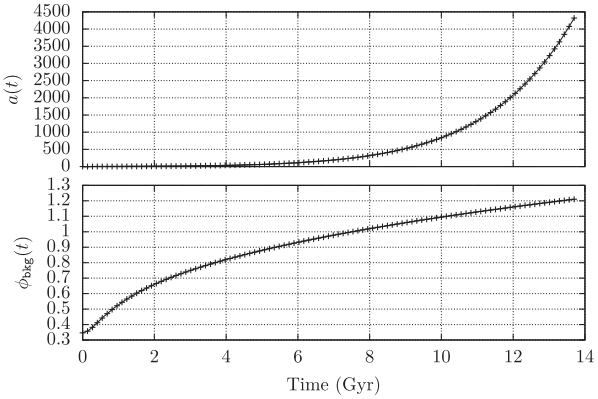

FIG. 5. Long-term cosmological evolution of the scale factor (upper panel) and background scalar field (lower panel) for a universe filled with quintessence ($H_i = 20H_0$).

This choice of gauge is made in order for the coordinate speed of light to remain finite throughout the integration [29]. Incidentally, setting $f = 1/3$ makes the Bona-Masso slicing equivalent to the conformal time gauge. In both slicings, the convergence of the method is beyond second order. The error is maximal at the center of coordinates but remains controlled throughout the integration.

We now study the case where the initial expansion factor is $H_i = 20H_0$, which is 1 order of magnitude larger than the Hubble factor today. The evolution of the scale factor and the homogeneous asymptotical value of the scalar field are shown in Fig. 5. The milder expansion between the two de Sitter phases happens earlier. As opposed to the previous case, the dominant part of the initial energy density is proportional to the gradient Ψ which in fact leads to a value of the density smaller than its asymptotical value. Figure 6 shows the evolution of the pulse on the spatial domain. The central value of the field does not return to its asymptotical value after the pulse is reflected. We have used geodesic slicing. The Hamiltonian violation profile is shown in Fig. 7. The convergence is again above second-order.

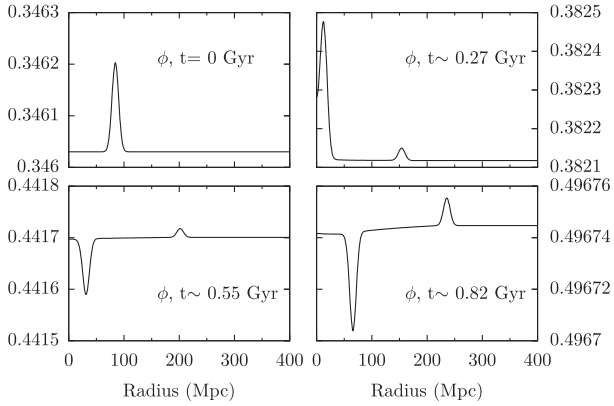

FIG. 6. Evolution of the radial profile of a Gaussian quintessence scalar pulse on a de Sitter background ($H_i = 20H_0$) for four different times ($t = 0$, 0.27, 0.55, and 0.82 Gyr).

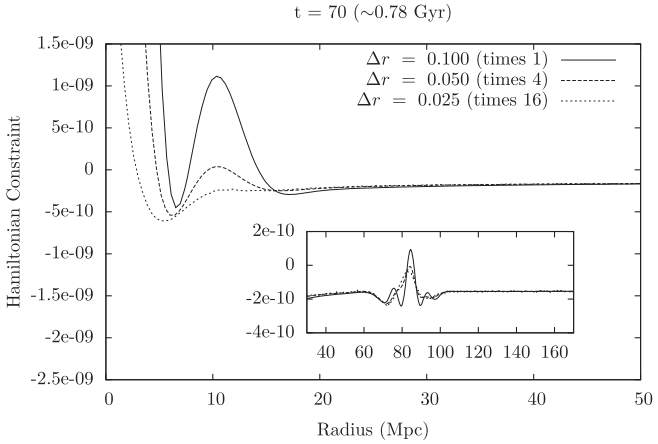

FIG. 7. Hamiltonian constraint violation profile resulting from the propagation of a Gaussian pulse in geodesic slicing for three values of the grid resolution at $t \sim 0.78$ Gyr, after the second scalar pulse has been reflected from the center of coordinates ($H_i = 20H_0$). The violation is maximal at the center of coordinates yet remains controlled throughout the integration. The rescaling of the constraint violation with resolution demonstrates that the convergence of the numerical scheme is above second order. The inset plot shows a close-up representation of the same quantity around the second scalar pulse after it has been reflected from the center of coordinates.

The fact that the central value of the field is different from the asymptotical value at late time has an impact on the local expansion around the center of coordinates. Figure 8 shows the trace of the extrinsic curvature tensor which is proportional to the opposite of the local isotropic expansion of space-time after the pulse has been reflected from the center. This shows how the expansion rate is smaller than that of the background at the center of coordinates which causes the local expansion to fall behind that of the background, thus creating a spherical space-time

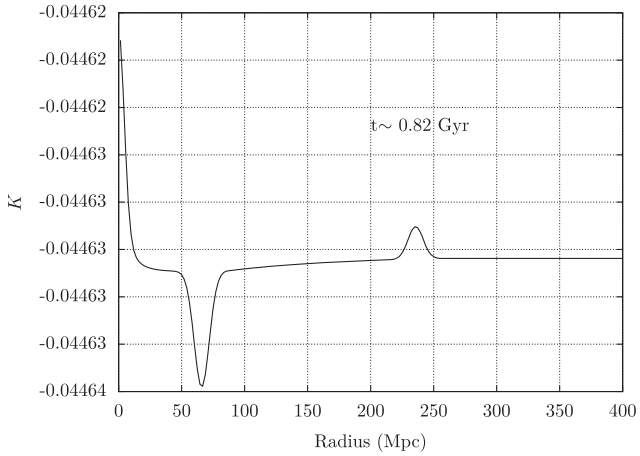

FIG. 8. Radial profile of the trace of the extrinsic curvature resulting from the propagation of a scalar pulse on a de Sitter background ($H_i = 20H_0$) at coordinate time $t \sim 0.82$ Gyr.

inhomogeneity region of mild expansion around the center of coordinates, an effect that is persistent and remains visible after the pulse is reflected.

V. COMPARISON WITH THE TOP HAT

We now turn to the comparison of our method to the top-hat model of spherical collapse. This is done for ΛCDM as well as the two quintessence models discussed earlier. The background evolutions are chosen as qualitatively similar to the evolution of our Universe, yet—as the fitting of the models onto the observed data is not our primary concern—the quintessence model parameters are chosen in order to display a significant departure from the ΛCDM model. Figure 9 shows the evolutions of the scale factor, the components of the energy density, and the equation-of-state parameter of the three considered backgrounds. The initial value of the scale factor is $a = 1$ in all models. The vertical dashed line corresponds to the point of zero redshift where the value of the Hubble factor equals the value measured today. The shaded regions of each plot correspond to times of negative redshift. The quantities ρ_m, ρ_Λ, and ρ_ϕ correspond to the value of the background energy density associated to dust, the cosmological constant, and quintessence, respectively. These are given in units in which $H_0 = 10^{-3}$. w_m, w_Λ, and w_ϕ denote the corresponding equation-of-state parameters.

The cosmological parameters used for each model are shown in Table I. The model-specific parameters for the RP potential are

$$n = 2,$$
$$M = \frac{2}{5}\left(\frac{3H_0^2}{8\pi}\right)^{1/(4+n)}(8\pi)^{\frac{n}{8+n}}. \tag{38}$$

The parameters of the PNGB model are

$$f = 15\pi/\sqrt{8\pi},$$
$$\mu = 6\left(\frac{3H_0^2}{8\pi}\right)^{1/4}. \tag{39}$$

These are chosen in order to produce acceleration at times close to the present day.

The comparison between the fully relativistic solution obtained by solving the complete set of BSSN equations and the top-hat solution is first studied by looking at the central value of the local scale factor defined as $a\psi^2(t, r = 0)$ in the BSSN coordinates. The quintessence field is assumed to be

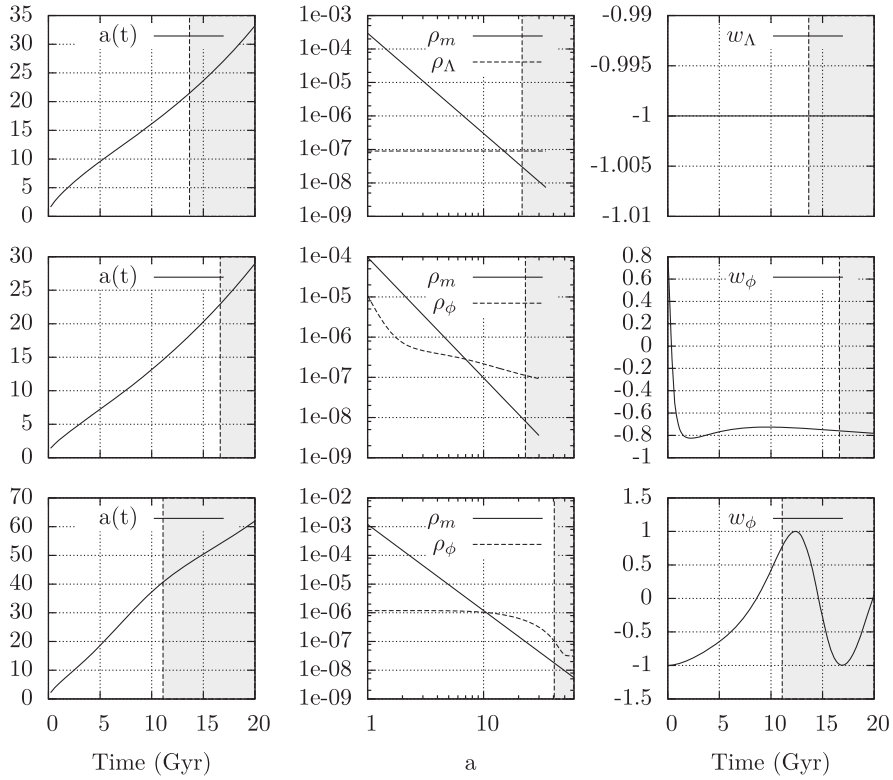

FIG. 9. Time evolution of the cosmological scale factor $a(t)$ (first column), the background densities associated to dust ρ_m, the cosmological constant ρ_Λ, and quintessence ρ_ϕ versus the cosmological scale factor (second column), and the time evolution of the corresponding equation-of-state parameters (third column) for the study of spherical collapse in the presence of quintessence. The upper row corresponds to the ΛCDM model, the middle row to the RP model of Eq. (28), and to the lower row to the PNGB model of Eq. (29).

TABLE I. Initial cosmological parameters employed to produce the simulations of Fig. 9.

Model	ΛCDM	RP	PNGB
Ω_m^i	0.9997	0.9	0.999
Ω_Λ^i	$1-\Omega_m^i$	0	0
Ω_ϕ^i	0	$1-\Omega_m^i$	$1-\Omega_m^i$
H_i	$50H_0$	$30H_0$	$100H_0$
$w_{\Lambda/\phi}^i$	-1	0.8	-1

homogeneous at initial time. The only perturbation to the homogeneous background comes from the matter energy density. We write the initial matter density contrast, $\delta_m \coloneqq (\rho_m/\bar{\rho}_m - 1)$ with $\bar{\rho}_m$ being the background matter density, as a step-like function in order to be close to the distribution of matter in the top-hat model:

$$\delta_m(t=0,r) = \delta_m^0\left(\frac{1}{2} - \frac{1}{2}\tanh(k(r-r_{\mathrm{span}}))\right), \qquad (40)$$

where δ_m^0 is the value of the density contrast at the center of coordinates and r_{span} is the radius at which it drops to half of its maximum value. The parameter k adjusts the steepness of the profile.

We take $r_{\mathrm{span}} \sim 20$ Mpc, which is of the order of the size of superclusters formed at late time in the history of the Universe. This can be considered as small compared to the size of the horizon yet sufficiently large to consider the inner value of the energy density to be homogeneous. As we have pointed out, the quintessence component should cluster very little on such scales. Our method allows us to test this *ab initio*. We compare the results of our computation with two realizations of the top-hat model in which the clustering parameter Γ is zero corresponding to a case where the quintessence is fully allowed to cluster (later referred to as "top-hat w.c.") and when it takes the form of Eq. (7) allowing no clustering at all (later referred to as "top-hat n.c."). We use geodesic slicing with zero shift, thus allowing a direct comparison of the metric components and ensuring identical time coordinates in both models.

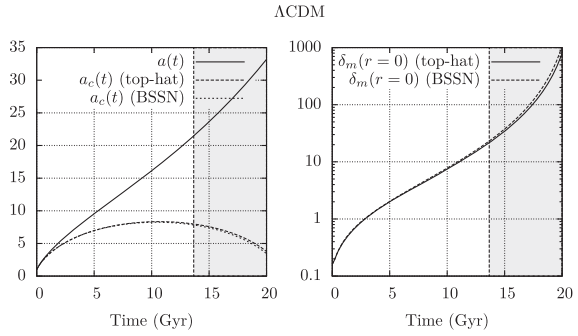

FIG. 10. In the left panel, we show the time evolution of the central value of the scale factor for the fully relativistic solution (dotted line), the central value for the top-hat solution in the ΛCDM model (dashed line), and the cosmological scale factor (solid line). In the right panel, we show the time evolution of the central value of the density contrast for the fully relativistic solution (dashed line) and the central value for the top-hat solution in the ΛCDM model (solid line).

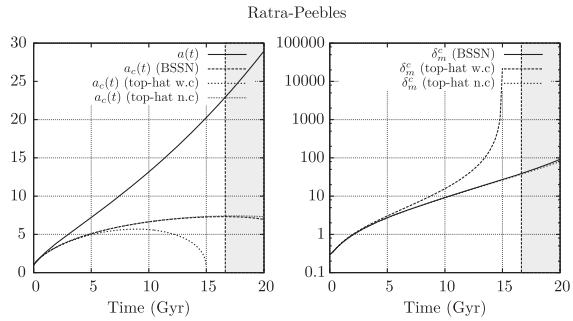

FIG. 11. In the left panel, we show the time evolution of the central value of the scale factor for the fully relativistic solution (dashed line), the central value for the top-hat solution in the RP model with complete clustering (short-dashed line) and without clustering (dotted line), and the cosmological scale factor (solid line). In the right panel, we show the time evolution of the central value of the density contrast for the fully relativistic solution (solid line) and the central value for the top-hat solution with complete clustering (dashed line) and without clustering (dotted line) in the RP model.

The evolution of the background and central values of the scale factor for the ΛCDM model are shown in Fig. 10 along with the density contrast at the center of coordinates. The initial value of the latter is fixed to $\delta_m(r=0) = 0.16$. In spite of the conceptual limitations of the top-hat model, this reproduces the correct relativistic predictions remarkably as far as the scale factor and contrast density are concerned. The correspondence is close to being exact up

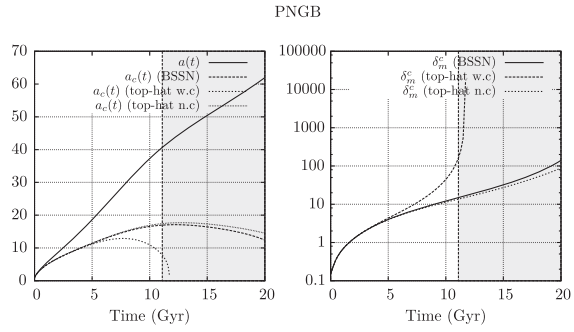

FIG. 12. In the left panel, we show the time evolution of the central value of the scale factor for the fully relativistic solution (dashed line), the central value for the top-hat solution in the PNGB model with complete clustering (short-dashed line) and without clustering (dotted line), and the cosmological scale factor (solid line). In the right panel, we show the time evolution of the central value of the density contrast for the fully relativistic solution (solid line) and the central value for the top-hat solution with complete clustering (dashed line) and without clustering (dotted line) in the PNGB model.

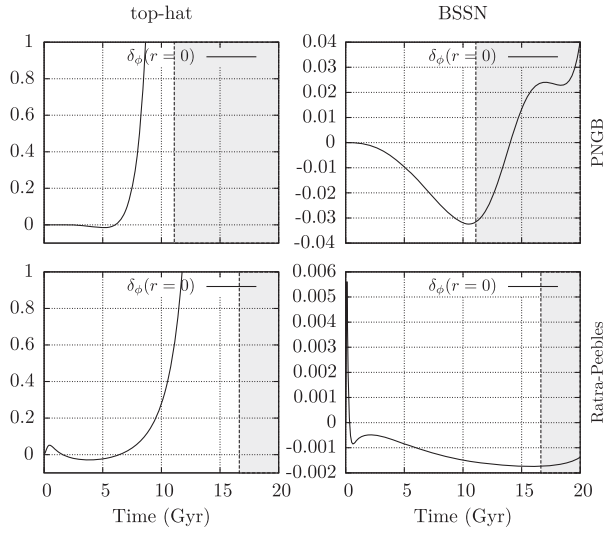

FIG. 13. Evolution of the central value of the quintessence energy density contrast during the collapse for the potentials of Eqs. (28) and (29). The left column shows the growth in the top-hat model with complete quintessence clustering. The right column shows the growth of the same quantity from the fully relativistic computation. The first row corresponds to the PNGB model, and the second row to the RP model.

to very deep within the nonlinear growth regime of δ_m. The same quantities are shown in Fig. 11 and Fig. 12 for the Ratra-Peebles and PNGB models, respectively, with initial density contrasts $\delta_m = 0.3$ and $\delta_m = 0.15$. The evolution of both the scale factor and the density contrast is really close to the top-hat solution at early time when the matter dominates over the quintessence field. When quintessence starts to dominate, the naive top-hat model with clustering predicts a quicker collapse than the relativistic solution. This solution remains close to the solution in both top-hat models without clustering at all times. The small departure from the top-hat model that is observed at late time for the PNGB potential could be an effect of a small yet nonzero late-time clustering of quintessence.

Figure 13 shows the central value of the quintessence density contrast, $\delta_\phi \coloneqq (\rho_\phi/\bar{\rho}_\phi - 1)$, with $\bar{\rho}_\phi$, for the top-hat model with clustering of quintessence and for the BSSN simulation for both models of quintessence. The top row corresponds to the PNGB model, while the second row corresponds to a Ratra-Peebles model. No *ad hoc* assumption is made regarding the Jeans length of the scalar field. We can see that the growth of the quintessence over-densities reaches its nonlinear regime while remaining bounded yet nonzero.

VI. BEYOND THE TOP-HAT MODEL

The method that we have developed allows us to explore the physical reasons behind the fact that quintessence clusters very little. The top-hat model—regardless of whether it allows quintessence to cluster—assumes that the over-dense region has the symmetries of the Friedmann-Lemaître-Robertson-Walker space-time. This forbids, in particular, the existence of anisotropic pressures and momentum transfers. While this is not a problem when only dust matter is present, this is rather arbitrary in the presence of quintessence. In the latter case, anisotropic pressure terms do build up values that are comparable to the inhomogeneous part of the isotropic pressure. However, the latter are themselves kept very small for other reasons.

In this section, we investigate the evolution of anisotropies during the collapse process for the PNGB and Ratra-Peebles models.

Spherical symmetry forbids any anisotropic quantities from being along directions other than the radial one. The momentum transfer associated to a scalar field is given by Eq. (21). It is useful to think of the scalar field as an imperfect fluid in order to identify the radial anisotropic pressure term as

$$\pi_\phi \coloneqq \pi^\phi_{rr} = (S^\phi_a - S^\phi_b). \tag{41}$$

This comes out as $\pi_\phi = \frac{\Psi^2}{\psi^4 a^2 \tilde{a}}$. It is zero in the background space-time, as it should be due to the vanishing of the quintessence gradient.

In order to understand why the field does not cluster, it is best to consider why it should collapse in the naive top-hat model ($\Gamma = 0$) in the first place. As it turns out, most of the difference in the energy density of the field comes from a difference in kinetic energy. Figure 14 shows the evolution of the effective quintessence equation-of-state parameter inside and outside of the over-dense region in this model for both the RP and PNGB models. This increases very quickly at early time, but this has a limited impact as dust matter is still the dominant component of the energy density. The corresponding increase in the quintessence kinetic energy is reinforced at the turnover when the over-dense region stops expanding and starts to collapse. This can be understood by considering Eq. (22) describing the evolution of the field momentum, which in the spatially homogeneous case reduces to

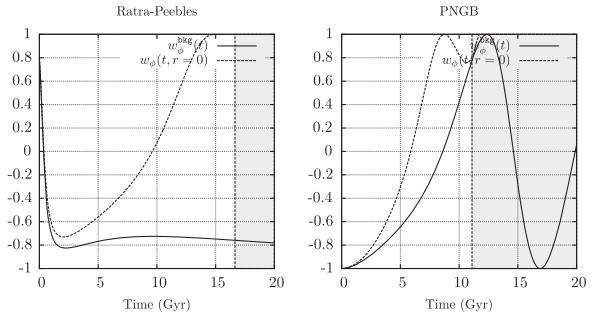

FIG. 14. Evolution of the central (dashed lines) and background (solid lines) values of the equation-of-state parameter in the RP (left panel) and PNGB (right panel) models in the naive top-hat picture in which quintessence fully clusters.

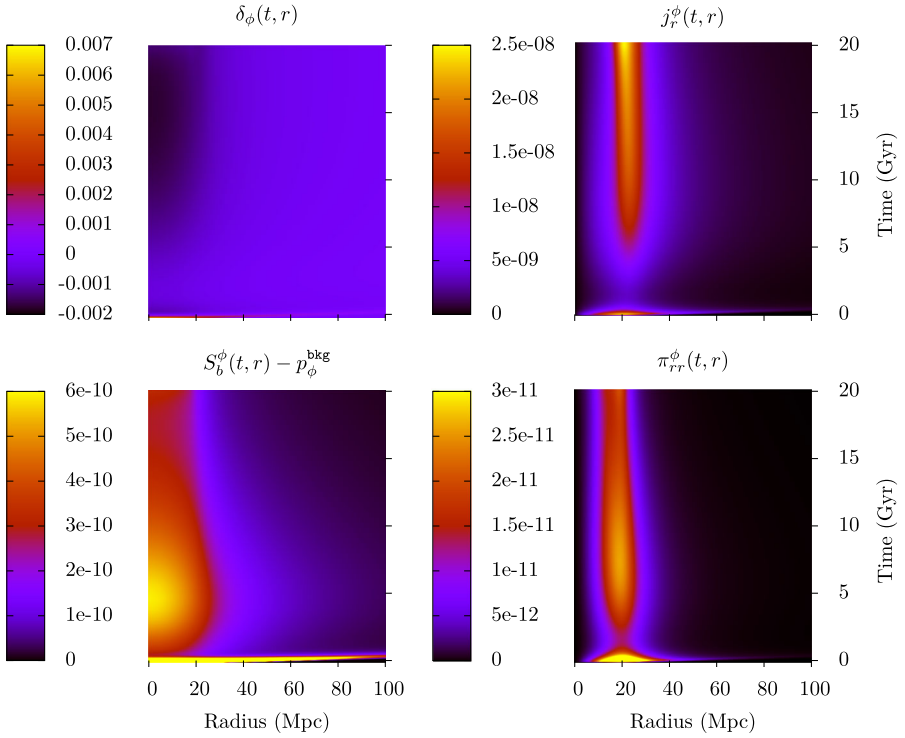

FIG. 15. Evolution of the anisotropies in the RP model. Top row: Field energy density contrast (left) and momentum transfer (right). Bottom row: Isotropic (left) and anisotropic (right) part of the field pressure.

$$\partial_t \Pi = K\Pi - \frac{dV}{d\phi}. \tag{42}$$

A collapsing space corresponds to $K > 0$, leading to a positive feedback on the growth of Π which can hardly be counterbalanced by the gradient of the potential, especially when the latter is very flat such as is the case in slow-roll expansion. The amount of kinetic energy built up within the over-dense region causes the quintessence field to act as stiff matter which accelerates the collapse.

The faulty part of this picture lies in the fact that the two parts of the space-time are completely disjoined and there is no possibility of momentum transfer between both regions. This transfer is made possible in the complete picture through the second term of Eq. (22). The modified top-hat model with no clustering reproduces this coupling artificially through the term proportional to Γ. This induces a loss of momentum proportional to the difference between the extrinsic curvatures of the inner and outer regions of space that effectively compensates the positive feedback effect described above. In reality, this term is purely phenomenological but is also nonlocal and Eq. (6) does not correspond to a solution of the equations of general relativity.

The method that we have developed to solve for the complete relativistic dynamics allows us to investigate what actually happens at the local scale.

The upper rows of Fig. 15 and Fig. 16 show the evolution of the field density contrast profile as a function of time along with the radial momentum transfer from the stress-energy tensor j_r^ϕ for the RP and the PNGB models, respectively. These figures were obtained with the same parameters as in the previous section. The results are presented in natural units with the Hubble constant value set to $H_0 = 0.001$.

As the over-dense region gets closer to the turnover, the momentum transfer increases to a large positive value corresponding to an outward transfer. This is responsible for balancing the kinetic energy inside and outside of the over-dense region. This transfer is maximal around the boundary of the over-dense region which is the place where the gradients of the scalar field and metric variables are maximal.

The decrease in the momentum of the field adjusts the equation-of-state parameter at the center of coordinates to its background value. As the universe approaches the vacuum-dominated era, this may either result in a more rapid or a delayed collapse depending on the shape of the potential. The PNGB model has a positive equation-of-state parameter at late time, resulting in a facilitated collapse which in turn increases the small value of the quintessence density contrast. In both models, this small yet nonzero density contrast induces a small difference of pressure inside the over-dense region. The bottom rows of Fig. 15 and Fig. 16 show the evolutions of the gradient of isotropic pressure between the over-dense and background regions (left panel) and the anisotropic pressure profiles (right panel). One sees that the isotropic pressure value dominates

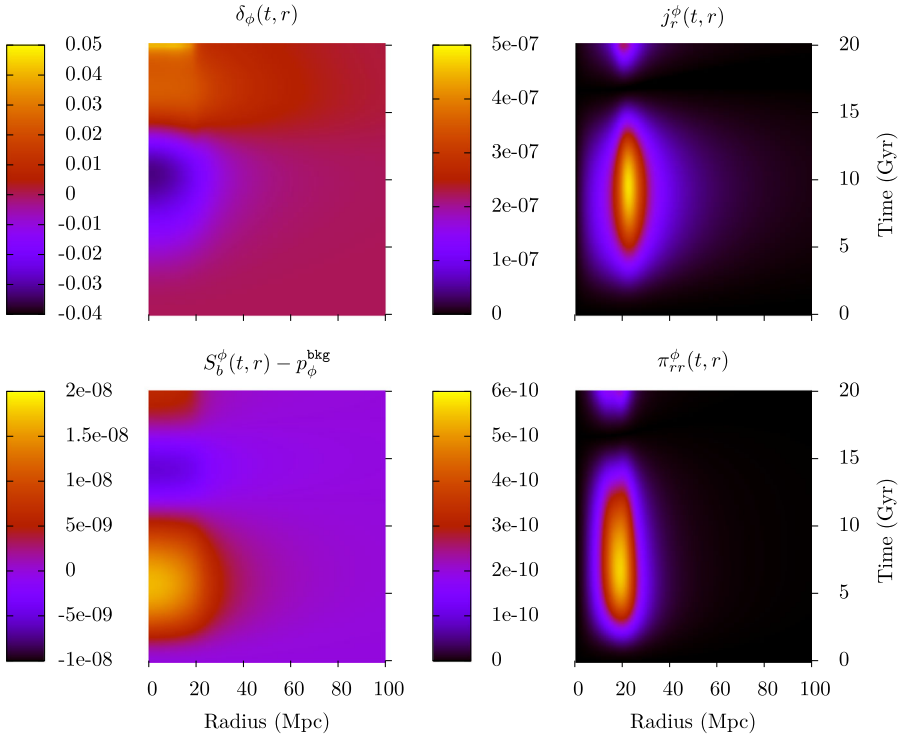

FIG. 16. Evolution of the anisotropies in the PNGB model. Top row: Field energy density contrast (left) and momentum transfer (right). Bottom row: Isotropic (left) and anisotropic (right) part of the field pressure.

over the isotropic pressure, yet the latter is 1 order of magnitude less than the anisotropic pressure around the boundary of the over-dense region where it is maximal.

For completeness, we ought to provide an explanation for the colors in the plots of Fig. 15 at early time. These are a consequence of the transient behavior following the evolution of the particular set of chosen initial conditions. At initial time, the field starts off in a very steep region of its potential. This results in a large gain of momentum at the center of coordinates which is not yet counterbalanced by the negative feedback of expansion or the momentum transfer which is initially null. The small increase in δ_ϕ that results, along with a positive equation of state $w_\phi \sim 1$, lead to a temporarily high pressure difference that overshoots the color scale of the plot. The effect is rapidly counterbalanced by expansion and momentum transfer. The small initial "jump" in the contrast density is perceivable in the two bottom plots of Fig. 13. One understands how the contrast density decreases more slowly in the top-hat picture with clustering as the only effect is the negative feedback from initial expansion. These transient behaviors have little effect on the overall evolution as these happen at a time when the matter energy density is dominant. However, these encourage us to look for more general initial conditions.

VII. CONCLUSION AND PERSPECTIVES

In this work we have proved the validity of a new method for solving the equations of evolution of a spherically symmetric cosmological space-time filled with a real quintessence scalar field. We have proved the stability and validity of our method by studying the evolution of a spherical distribution of quintessence inhomogeneity on a de Sitter background. This allowed us to study the deviation of the local expansion around quintessence over-densities in formation and opens perspectives of more detailed study of the backreactions of local distributions of energy on the cosmological expansion.

We have shown how the method can be used to study the impact of quintessence on the spherical collapse of a matter over-density. We have undertaken this study for three different cosmological backgrounds and compared our results to those obtained in the top-hat picture. It turns out that the top-hat model predicts evolutions of the scale factor relatively close to the solution obtained using the fully relativistic method when the quintessence field is artificially kept homogeneous. The solution diverges slightly at the end of the integration when small over-densities do build up. We have identified the cause of the overall great homogeneity of the quintessence field as the existence of a non-null momentum transfer and anisotropic pressure component of the stress-energy tensor that are maximal at the boundary of the spherical over-density.

We see the present work as a first step towards a more systematic study of the impact of the shape of the quintessence potential on the physics of galaxy clusters. It would be interesting to look at the evolution of geodesics

near the boundary of the forming object. Even though the anisotropic terms are small, we expect that these might have an effect in the context of scalar-tensor theories where these are expected to couple directly to space-time curvature. In most treatments of spherical collapse, the top-hat model is assumed to be valid up to a time when it is assumed that the structure gets virialized. The top-hat model does not allow one to account for the process and the argument of virialization is used as a workaround and not as a prediction. We did not need this assumption in the present work. A generalization of our method to varieties of energies with more general equations of state would be an interesting task that could ultimately allow us to investigate the physics of the very late stages of the evolution, just before the collapse.

ACKNOWLEDGMENTS

J. R. is supported by a FRS-FNRS (Belgian Fund for Scientific Research) Research Fellowship. A. F. is partially supported by the ARC convention No. 11/15-040. I. C.-C. acknowledges support from the European Research Council (ERC) through the Starting Independent Research Grant CAMAP-259276. This work was also supported by the Spanish Government AYA2013-40979-P) and the local Autonomous Government (Generalitat Valenciana, grant Prometeo-II/2014/069). Computations were performed at the "plate-forme technologique en calcul intensif" (PTCI) of the University of Namur, Belgium, with the financial support of the FRS- FNRS (conventions No. 2.4617.07. and No. 2.5020.11).

APPENDIX: PIRK OPERATOR SPLITTING FOR SCALAR FIELD EQUATIONS

The operator splitting for the space-time quantities is the same as the one used in Ref. [1]. The Ψ function is evolved explicitly. The Π function is evolved semi-implicitly using the following splitting:

$$L_{2(\Pi)} = \frac{\alpha}{a^2\psi^4\hat{a}}\Psi\left(\frac{2}{r} - \frac{\partial_r\hat{a}}{\hat{a}} + \frac{\partial_r\alpha}{\alpha} + 2\frac{\partial_r\psi}{\psi}\right), \tag{A1}$$

$$L_{3(\Pi)} = \alpha K\Pi + \frac{\alpha}{a^2\psi^4\hat{a}}\partial_r\Psi - \alpha\frac{dV}{d\phi}. \tag{A2}$$

These quantities are evolved prior to the auxiliary BSSN quantity $\hat{\Delta}^r$, the evolution scheme of which remains unchanged.

[1] J. Rekier, I. Cordero-Carrión, and A. Füzfa, Phys. Rev. D **91**, 024025 (2015).
[2] A. G. Riess *et al.* (Supernova Search Team), Astron. J. **116**, 1009 (1998).
[3] S. Perlmutter *et al.* (Supernova Cosmology Project), Astrophys. J. **517**, 565 (1999).
[4] A. G. Riess *et al.* (Supernova Search Team), Astrophys. J. **560**, 49 (2001).
[5] M. Kowalski *et al.* (Supernova Cosmology Project), Astrophys. J. **686**, 749 (2008).
[6] R. Amanullah *et al.*, Astrophys. J. **716**, 712 (2010).
[7] E. Komatsu *et al.* (WMAP Collaboration), Astrophys. J. Suppl. Ser. **180**, 330 (2009).
[8] P. A. R. Ade *et al.* (Planck Collaboration), arXiv:1502.01590.
[9] L. Guzzo *et al.*, Nature (London) **451**, 541 (2008).
[10] S. Weinberg, Rev. Mod. Phys. **61**, 1 (1989).
[11] E. J. Copeland, M. Sami, and S. Tsujikawa, Int. J. Mod. Phys. D **15**, 1753 (2006).
[12] B. Ratra and P. J. E. Peebles, Phys. Rev. D **37**, 3406 (1988).
[13] C. Wetterich, Nucl. Phys. **B302**, 668 (1988).
[14] J.-M. Alimi *et al.*, in *Proceedings of the International Conference on High Performance Computing, Networking, Storage and Analysis, Salt Lake City, UT, USA November 11–15, 2012* (IEEE, New York, 2012).
[15] V. R. Bouillot, J.-M. Alimi, P.-S. Corasaniti, and Y. Rasera, Mon. Not. R. Astron. Soc. **450**, 145 (2015).
[16] V. Springel *et al.*, Nature (London) **435**, 629 (2005).
[17] L. Wang and P. J. Steinhardt, Astrophys. J. **508**, 483 (1998).
[18] G. M. Voit, Rev. Mod. Phys. **77**, 207 (2005).
[19] C. Horellou and J. Berge, Mon. Not. R. Astron. Soc. **360**, 1393 (2005).
[20] L. R. Abramo, R. C. Batista, L. Liberato, and R. Rosenfeld, Phys. Rev. D **023516**, 1 (2009).
[21] R. A. A. Fernandes, J. P. M. de Carvalho, A. Y. Kamenshchik, U. Moschella, and A. da Silva, Phys. Rev. D **85**, 083501 (2012).
[22] W. Li and L. Xu, Eur. Phys. J. C **74**, 2870 (2014).
[23] D. Mota and C. van de Bruck, Astron. Astrophys. **421**, 71 (2004).
[24] N. J. Nunes and D. F. Mota, Mon. Not. R. Astron. Soc. **368**, 751 (2006).
[25] N. Wintergerst and V. Pettorino, Phys. Rev. D **82**, 103516 (2010).
[26] E. Bertschinger and P. Zukin, Phys. Rev. D **78**, 024015 (2008).
[27] B. Chang, J. Lu, and L. Xu, Phys. Rev. D **90**, 103528 (2014).
[28] M. Shibata and M. Sasaki, Phys. Rev. D **60**, 084002 (1999).
[29] J. M. Torres, M. Alcubierre, A. Diez-Tejedor, and D. Núñez, Phys. Rev. D **90**, 123002 (2014).
[30] M. Alcubierre, A. de la Macorra, A. Diez-Tejedor, and J. M. Torres, Phys. Rev. D **92**, 063508 (2015).

[31] T. Padmanabhan, *Structure Formation in the Universe* (Cambridge University Press, Cambridge, England, 1993).
[32] N. Weinberg and M. Kamionkowski, Mon. Not. R. Astron. Soc. **341**, 251 (2003).
[33] R. R. Caldwell, R. Dave, and P. J. Steinhardt, Phys. Rev. Lett. **80**, 1582 (1998).
[34] J.-c. Hwang and H. Noh, Phys. Rev. D **64**, 103509 (2001).
[35] P. D. Lasky and A. W. Lun, Phys. Rev. D **75**, 024031 (2007).
[36] T. Nakamura, K. Oohara, and Y. Kojima, Prog. Theor. Phys. Suppl. **90**, 1 (1987).
[37] M. Shibata and T. Nakamura, Phys. Rev. D **52**, 5428 (1995).
[38] T. W. Baumgarte and S. L. Shapiro, Phys. Rev. D **59**, 024007 (1998).
[39] T. W. Baumgarte and S. Shapiro, *numerical relativity: Solving Einstein's Equations on the Computer* (Cambridge University Press, Cambridge, England, 2010).
[40] É. Gourgoulhon, *3+1 Formalism in general relativity: Bases of Numerical Relativity* (Springer, New York, 2012).
[41] R. Wald, *general relativity* (University of Chicago, Chicago, 2010).
[42] M. Alcubierre, *Introduction to 3+1 numerical relativity* (Oxford University, New York, 2008).
[43] I. Cordero-Carrión and P. Cerdá-Durán, arXiv:1211.5930.
[44] I. Cordero-Carrión and P. Cerdá-Durán, in *Advances in Differential Equations and Applications*, edited by F. Casas and V. Martínez (Springer, New York, 2014), p. 267.
[45] J. A. Frieman, C. T. Hill, A. Stebbins, and I. Waga, Phys. Rev. Lett. **75**, 2077 (1995).
[46] L. Amendola and S. Tsujikawa, *Dark Energy: Theory and Observations* (Cambridge University Press, Cambridge, England, 2010).